

---

# Simultaneous Recovery of Size and Radioactivity Concentration of Small Spheroids with PET Data

Chi-Hsien Chen, Raymond F. Muzic, Jr., A. Dennis Nelson and Lee P. Adler

*Department of Biomedical Engineering and Department of Radiology, Case Western Reserve University, Cleveland; and Division of Nuclear Medicine University Hospitals of Cleveland, Ohio*

---

Quantification of tumor activity is used to predict prognosis and discriminate benign from malignant lesions identified by PET. Accurate quantitation of small lesions requires correction for the partial volume effects. Such a correction is often based on the recovery coefficient (RC), which depends on the lesion size, the object-to-background ratio (OBR) and physical properties of the media. The purpose of this investigation was to determine whether a model-based optimization method to simultaneously recover the size and the activity concentration of small spheroids could improve estimates of lesion radioactivity when object size is unknown. For reference, we compared our method with a widely used approach, RC correction, that requires the object size to be known. **Methods:** A three-dimensional, spatially varying, object size- and contrast-dependent Gaussian model of the point spread function (PSF) of an ECAT EXACT was developed. The observed dependence of the PSF on random coincidences and measured-peak/background activity were included in the PSF using three adjusting factors. Size and radioactivity concentration of a spheroid were estimated by adjusting size and concentration until model output best matched the image data. Elliptic and circular phantoms both containing seven hot spheroids, with OBRs ranging from 5.6 to 0 background, were evaluated. **Results:** The proposed quantification method reduced the activity error by 11%–63% of the error obtained without correction. The greatest error reduction occurred for small spheroids. The average error in radius estimation ranged from 2% to 48%, wherein the smallest spheroid produced the largest errors. For spheroids with diameters from 8 to 22 mm, Student *t* test (paired, one-tail) showed the proposed method significantly improved accuracy ( $P < 0.05$ ) in comparison with the RC method and also in comparison with optimization without the three adjusting factors. **Conclusion:** The model-based optimization method improved estimation of radioactivity concentration over that corrected by the RC method and that made without any correction. It also provided accurate estimation of size for spheroids larger than 6 mm in diameter.

**Key Words:** model-based optimization; partial-volume effect; small tumor; PET

**J Nucl Med 1999; 40:118–130**

---

Received Dec. 26, 1997; revision accepted Jun. 4, 1998.

For correspondence or reprints contact: Lee P. Adler, MD, Nuclear Medicine, Wake Forest University School of Medicine, Medical Center Blvd., Winston-Salem, NC 27157-1088.

**R**ecent studies have shown that PET with  $^{18}\text{F}$ -2-fluorodeoxy-D-glucose (FDG) is very useful in differentiating between benign and malignant conditions, tumor staging, diagnosis of posttreatment recurrence, determination of responses to therapy and assessment of prognostic factors (1–10). Most of these applications take advantage of the capability of PET to quantify tissue radioactivity concentration. One of the major limitations to quantitative accuracy is caused by limited spatial resolution (7,11–15). Experimental data collected on an ECAT EXACT (Siemens/CTI, Knoxville, TN) have shown that the ratio of peak measured to true radioactivity, also called recovery coefficient (RC) (3,11,12), is 0.76 for a 22-mm inner diameter hot spheroid with object-to-background ratio (OBR) of 12.6 in a water-filled  $30.5 \times 22.3$ -cm diameter elliptical cylinder (16). For a 6.4-mm inner diameter hot spheroid, under the same conditions, the RC drops to 0.13. This underestimation of radioactivity is conventionally called partial-volume effect (PVE).

Two traditional approaches have been used to correct for PVE. The first traditional approach incorporates PVE into a tracer kinetic model so that the PVE is estimated along with the physiologic function parameters (14,17–20). This approach is applicable only to dynamic studies when the data are analyzed using a mathematical model. Neither dynamic data nor a model are usually available in applications such as radioactivity quantification in tumors.

The second traditional approach to account for PVE uses anatomic information and a model of the scanner spatial resolution characteristics to estimate the true tracer concentration (3,21–27). This approach often cannot be used because of the requirement of anatomic data from which structure size is determined. Without these data, the techniques are of limited value because even small errors in size have been observed to cause large errors in the estimation of blood flow (17). Moreover, the methods proposed (23,25,26) require MRI data to be segmented and registered with PET data. This can be time consuming and prone to error.

Yu et al. (28) have proposed a nontraditional approach that uses model-based optimization to simultaneously esti-

mate width and activity of the putamen in  $^{18}\text{F}$ -L-6-fluorodopa PET studies. They assumed there was no variation in tracer uptake along the axial direction and that the structure was long in one in-plane direction. Consequently, a one-dimensional Gaussian point spread function (PSF) was used to estimate and correct for PVE. Though the results were good, Yu et al. (28) acknowledged that the approach is most applicable when the structure width is larger than the full width at half maximum (FWHM) of the PSF and when structures similar in shape to putamen are considered. Because detection of tumors or lymph node metastasis often involves objects smaller than FWHM of the system PSF and because the size of tumors, unlike putamen, could change over a wide range, their method is not generally applicable to oncology studies.

In this article, we consider tumor quantification for oncology applications. We take a similar approach to that described by Yu et al. (28) but use a three-dimensional model. The three-dimensional model is based on a simplified approximation of a previously developed PSF model that accounts for both scattered coincidences and partial volume effects (16). We also propose that the FWHM of the PSF should be adjusted on the basis of the readily available peak-to-background ratio (apparent contrast) and randoms ratio, because we have experimentally observed such a dependence. Our approach eliminates the inconvenience, time and cost of obtaining anatomic data for the structure of interest. For reference, a simple RC correction method using known object size is compared with the proposed approach. In addition, the importance of the model-data discrepancy for small objects and limitations of this approach are explored.

## MATERIALS AND METHODS

### Theory

The relationship between the PSF of the PET scanner, the object ( $O$ , the true spatial distribution of radioactivity concentration) and the theoretical radioactivity concentration distribution in the reconstructed image ( $I$ ), can be modeled by

$$I(\vec{x}) = \int O(\vec{\alpha})PSF(\vec{x}, \vec{\alpha}, O)d\vec{\alpha}, \quad \text{Eq. 1}$$

where  $\vec{x}$  is a three-element vector,  $[x, y, z]^T$ , representing a point in the three-dimensional space. The dimensionality of  $\vec{\alpha}$ , which serves as a dummy variable of integration, depends on how  $PSF$  is defined. The  $O$  in  $PSF(\vec{x}, \vec{\alpha}, O)$  is used to emphasize that the PSF is object dependent.

Previously, we developed a nonlinear, spatially variant, object-dependent (NLSVOD) PSF function that consists of three Gaussian functions and five other simple functions with a total of 24 parameters (16). The NLSVOD model accounts for plane sensitivity variation, object-dependent scattered photons and the spatially varying resolution of the scanner. Although the model calculation of a pixel value takes only approximately 1.5 s, more than one hundred thousand pixels may need to be calculated in the model-based optimization approach, which could take days. To reduce the computation time, the generalized superposition integral in Equation 1 is replaced by convolution, and  $PSF(\vec{x}, \vec{\alpha}, O)$  is approxi-

mated by a three-dimensional Gaussian function multiplied with a scatter scaling factor. The implicit assumption behind this approximation is that the shift-variance of the  $PSF(\vec{x}, \vec{\alpha}, O)$  is neglected within a small volume of interest (see the assumptions about object,  $O$ , and the description of the volume of interest,  $V$ , below). This approximation will be referred to as ‘‘scaled Gaussian model’’ and is given by

$$I(\vec{x}) \cong s_s(O) \int O(\vec{\beta})PSF_G(\vec{x} - \vec{\beta})d\vec{\beta}, \quad \text{Eq. 2}$$

where  $\vec{\beta}$  is a three-element vector,  $[x', y', z']^T$ ,  $PSF_G$  is the three-dimensional Gaussian function

$$PSF_G(x - x', y - y', z - z') = \frac{1}{(2\pi)^{3/2}\sigma_{xy}^2\sigma_{gz}} e^{-1/2\left(\frac{(x-x')^2 + (y-y')^2}{\sigma_{xy}^2} + \frac{(z-z')^2}{\sigma_{gz}^2}\right)}, \quad \text{Eq. 3}$$

and  $s_s(O)$  is the scatter scaling factor defined as

$$s_s(O) = \frac{\int O(\vec{\alpha})PSF(\vec{x}, \vec{\alpha}, O)d\vec{\alpha}}{\int O(\vec{\beta})PSF_G(\vec{x} - \vec{\beta})d\vec{\beta}} \Big|_{\vec{x}=\vec{x}_c}, \quad \text{Eq. 4}$$

where  $\vec{x}_c$  is the point of interest.

We assume that (a) the object function  $O$  can be approximated by a sphere  $O_{sp}$  in a warm or cold background; (b) the radioactivity inside the sphere is uniform; (c) the background level is uniform; and (d) the dimension of the background in any direction is large compared with the standard deviations  $\sigma_{xy}$  and  $\sigma_{gz}$  in Equation 3. With these assumptions, Equation 2 can be simplified to

$$I(\vec{x}) \cong s_s(O)[O_{sp}(r, \vec{x}_c, \vec{x}) - B_{sp}(r, \vec{x}_c, \vec{x}) \otimes PSF_G(\vec{x})] + B, \quad \text{Eq. 5}$$

where  $\otimes$  is convolution,  $B$  is the background tracer concentration,  $r$  and  $\vec{x}_c$  are the radius and the center of the sphere, respectively, and

$$O_{sp}(r, \vec{x}_c, \vec{x}) = \begin{cases} A_{sp} & \text{if } \|\vec{x} - \vec{x}_c\| \leq r \\ 0 & \text{otherwise} \end{cases}, \quad \text{Eq. 6}$$

where  $\|\vec{x}\|$  denotes the length of the vector  $\vec{x}$ .  $A_{sp}$  is the tracer concentration inside the sphere and

$$B_{sp}(r, \vec{x}_c, \vec{x}) = \begin{cases} B & \text{if } \|\vec{x} - \vec{x}_c\| \leq r \\ 0 & \text{otherwise} \end{cases}. \quad \text{Eq. 7}$$

Note that  $s_s(O)$  can be evaluated for a single pixel and both  $O_{sp}$  and  $PSF_G$  have analytical formulas for their Fourier transforms, so the convolution in Equation 5 can be calculated very efficiently in the frequency domain.

If all of the other parameters for functions  $PSF$ ,  $PSF_G$  and  $O$  are known, then  $r$ ,  $\vec{x}_c$ ,  $A_{sp}$  and  $B$  can be estimated by minimizing the objective function

$$\Phi(r, \vec{x}_c, A_{sp}, B) = \sum_{\vec{x} \in V} [I_m(\vec{x}) - I(\vec{x})]^2 + \sum_j \xi_j(r, \vec{x}_c, A_{sp}, B), \quad \text{Eq. 8}$$

where  $I_m(\vec{x})$  is the measured pixel value,  $V$  is the volume of a cube that just covers the whole sphere of interest and  $\xi_j(r, \vec{x}_c, A_{sp}, B)$  is a

penalty function used to define simple constraints of upper or lower bounds (Equation 31 in Spang [29]).

Based on analysis of measured data (see Results), three adjusting factors,  $f_{nm}$ ,  $f_{Rxy}$  and  $f_{Rz}$ , are added to Equation 3:

$$PSF_G(x - x', y - y', z - z') = \frac{f_{nm}}{(2\pi)^{3/2} f_{Rxy}^2 \sigma_{Rxy}^2 f_{Rz}^2 \sigma_{Rz}^2} e^{-1/2 \left( \frac{(x-x')^2 + (y-y')^2}{f_{Rxy}^2 \sigma_{Rxy}^2} + \frac{(z-z')^2}{f_{Rz}^2 \sigma_{Rz}^2} \right)}, \quad \text{Eq. 9}$$

where  $f_{nm}$ ,  $f_{Rxy}$  and  $f_{Rz}$  can be empirically modeled as functions of apparent contrast,  $AC = I(\bar{x}_c)/B$ , and randoms ratio,  $RR = \text{randoms/total events}$ :

$$f_{xxx} = k_b - k_c e^{-k_d(AC - k_d)} - k_e RR, \quad xxx \in \{nm, gxy, gz\}, \quad \text{Eq. 10}$$

where  $k_a, k_b, \dots, k_e$  are the parameters for the adjusting factors. This approach will be referred to as "AC-RR-adjusted model."

### Data Collection

A 21.5-cm circular and a 30.5 × 22.3-cm elliptical cylinder from Data Spectrum Corporation (Hillsborough, NC) were used in this study. Data were collected in two-dimensional (septa extended) mode with an ECAT EXACT (30). All the images were reconstructed with Hann filter, cutoff 0.4. Other reconstruction details and the resulting image size, pixel size and center-to-center distance between image planes were the same as described in Chen et al. (16). The calibration of true activity concentrations and the scanner calibration were also performed in the same way as described by Chen et al. (16).

There were two major data groups. Group I was used to determine parameters of the AC-RR-adjusted model and had long emission and transmission acquisition durations. Group II was the test group. The model-based optimization was applied on this group to simultaneously estimate the spheroid radius and the radioactivity concentration. This group had short emission and transmission acquisition durations comparable to those of a clinical oncologic PET study. Group II was further divided into four subgroups (Table 1), depending on which phantom and spheroids were used and also depending on whether special treatment was performed during the filling of the spheroids or during data acquisition.

**Group I.** Seven fillable spheroids (Data Spectrum Corporation) with average inner diameters of 34, 22, 16, 14, 10, 8.3 and 6.4 mm were used in this group. These spheroids were all filled with the same concentration of <sup>18</sup>F and were put into the elliptical cylindri-

cal phantoms with warm background. The largest spheroid was always in the center of the phantom, and the others were 6.8–8.4 cm from the center. The positions of these smaller spheroids were not always the same on different occasions, and no specific efforts were made to keep them in or out of the same plane. A typical arrangement is as shown in Chen et al. (16).

All of the emission scans in this group were acquired overnight and had acquisition durations of at least 11 h. After the emission scan, when the maximal background activity was less than 0.12 kBq/mL and before moving the phantom, a transmission scan with acquisition duration of at least 80 min was performed. There were five studies with contrast ranging from 67.8 to 5.56 in this group.

**Group IIA.** This subgroup used the same elliptical phantom and spheroids as those used in group I. The data of this subgroup were actually collected immediately before the data collection of group I. A 15-min transmission scan without the spheroids was acquired first. Then the spheroids were filled with activity and put into the elliptical phantom. Appropriate radioactivity was also added to the background, and a 15-min emission scan was acquired. Note that for this data group the phantom positions for the transmission and the emission scan might not be exactly the same. This was by design to emulate the imperfect registration that often occurs in clinical studies.

**Group IIB.** The circular phantom was used in this subgroup. The spheroids were the same as those used in group IIA, except that the 14-mm inner diameter spheroid was replaced by a 4.0-mm spheroid. A 45-min transmission scan without spheroids was performed before a series of emission scans. The background activity was initially zero, and the acquisition duration for each emission scan was 20 min. After the first acquisition, radioactivity was added to and mixed well with the background solution. For the subsequent four acquisitions, the OBRs ranged from approximately 30:1 to 8:1.

**Group IIC.** The same procedure as in group IIB was repeated with the circular phantom replaced by the elliptical one, and the acquisition durations for both transmission and emission scans were reduced to 15 min.

**Group IID.** Two studies were included in this subgroup. The phantom, spheroids and data acquisition procedure were exactly the same as those used in group IIA. The phantom was purposefully shifted 13 mm horizontally within the image plane between the transmission and emission scan in one experiment. In the other experiment, bubbles or extra <sup>18</sup>F solution were purposefully introduced into the spheroids depending on the spheroid structure

**TABLE 1**  
Summary of Acquisition Conditions for Different Data Groups

Data groups	Acquisition time (min)		Phantom type	Sphere radius (mm)		Bubbles or extra fluid	T-E misregistration	No. of studies*
	Emission	Transmission		2.0	6.9			
I	>660	>80	Elliptic	No	Yes	No	No	5
IIA	15	15	Elliptic	No	Yes	No	Yes	5
IIB	20	45	Circular	Yes	No	No	Yes	5
IIC	15	15	Elliptic	Yes	No	No	Yes	5
IID	15	15	Elliptic	No	Yes	Yes†	Exaggerated†	2

\*Different studies in the same group have quite different object-to-background ratios except group IID.

†Applied on one of the two studies in this group but not on both.

T-E = transmission-emission.

(Fig. 1). The volume of the bubble or the extra solution in a spheroid ranged from 6.5% to 40% of the volume of the spheroid.

### Fitting of the Adjusting Factors

Spheroids smaller than 16 mm in diameter in group I were used to estimate parameters  $k_a, k_b, \dots, k_e$  of the three adjusting factors. The spheroid center  $\bar{x}_c$  was estimated by setting the three adjusting factors to 1, setting  $r, A_{sp}, B$  to their known values and finding the  $\bar{x}_c$  that minimizes Equation 8 using a Marquardt-Levenberg method. Using this value of  $\bar{x}_c$  and other known parameter values ( $r, A_{sp}$  and  $B$ ), the three adjusting factors were determined by minimizing the objective function

$$\Phi'(f_{nm}, f_{gxy}, f_{gz}) = \sum_{\bar{x} \in V} [I_m(\bar{x}) - I(\bar{x})]^2 + \sum_k \xi'_k(f_{nm}, f_{gxy}, f_{gz}) \quad \text{Eq. 11}$$

under the constraint that the three adjusting factors are larger than zero.  $\xi'_k(f_{nm}, f_{gxy}, f_{gz})$  is a penalty function defined in a similar way as in Equation 8. Only those conditions in which the adjusting factors made  $f_{gz}$  a monotonic function of  $AC$  were chosen to determine the parameters  $k_a, k_b, \dots, k_e$  in Equation 10 (see Results and Discussion).

### Initial Guess

After the parameters  $k_a, k_b, \dots, k_e$  were obtained, model-predicted activity profiles for spheroids of different radii at a contrast ratio of 10 and a randoms ratio of 0.1 were calculated by an iterative scheme. The FWHMs of these model-predicted activity profiles for different spheroid radii were calculated and stored in a look-up table. Before the optimization, FWHMs of the unsmoothed images of the spheroid of interest along the  $x, y$  and  $z$  directions (Figure 4 in Chen et al. [16]) were calculated, and their mean was compared with the look-up table to determine an initial estimate of the spheroid radius,  $r_0$ . The initial guesses of the spheroid center,  $\bar{x}_{c0}$ , and of the background activity,  $B_0$ , were obtained based on the location of the activity peak and by fitting the sum of a one-dimensional Gaussian function and a line to the activity profiles. The initial guess of the true activity of the spheroid,  $A_{sp0}$ , could then be estimated by

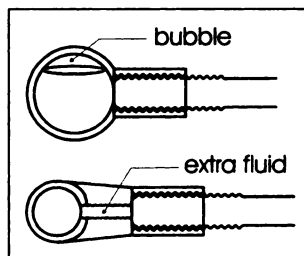
$$A_{sp0} = \frac{p - B_0}{c} + B_0, \quad \text{Eq. 12}$$

where  $p$  is the peak value measured near  $\bar{x}_c$  and  $c$  is the model-predicted RC when  $B = 0, r = r_0$  and  $\bar{x}_c = \bar{x}_{c0}$ .

### Model-Based Optimization

A volume of interest in the shape of a cube that covers the whole spheroid of interest was positioned manually on images of group II data. The location of the peak voxel within the cube was

**FIGURE 1.** Special treatment for one experiment in group IID. For spheroids larger than 10.4-mm diameter, which have structure shown at top, an air bubble was introduced. For smaller spheroids, which have structure shown at bottom, extra  $^{18}\text{F}$  solution was filled in stem space.



determined. Typically the length of each cube edge was a little bit more than twice the FWHM of the activity profile through the peak voxel. Empirically, when the randoms ratio was larger than 0.05, the reconstructed images were convolved with a one-dimensional Gaussian function with standard deviation 3.4 mm along the axial direction to reduce statistical noise. The raw or smoothed image data within the cube and the initial guesses described in the previous section were input to an optimization program to estimate values of the parameters  $r, \bar{x}_c, A_{sp}$  and  $B$ . This program was based on a numerical analysis routine that used the principle axis method to locate the minimum of a multivariate function (31,32). We constrained  $r$  to be larger than 2 mm and smaller than the minimum of one and a half times  $r_0$  and  $r_0$  plus one pixel width. Other constraints were that activities must be larger than or equal to zero and  $\|\bar{x}_c - \bar{x}_{c0}\| \leq \sqrt{2pw^2 + pt^2}$ , where  $pw$  is the pixel width and  $pt$  is the image plane thickness.

### Comparison with Scaled Gaussian Model

The same procedure used for the model-based optimization section was repeated, except that all three adjusting factors were set to unity to investigate the importance of these adjusting factors.

### Comparison with Simple RC Method

Parameters  $\bar{x}_c, A_{sp}$  and  $B$  for group II data were estimated as previously described in the model-based optimization section, except that  $r$  was treated as a known parameter. The results were compared with the results obtained by a simple RC method (3). This RC method assumes that theoretical RC,  $RC_t$ , is a function of the volume of a spheroid:

$$RC_t = a \log V_{sp} + b. \quad \text{Eq. 13}$$

Parameters  $a$  and  $b$  in Equation 13 were obtained by fitting the measured RC values in group I with OBR 9.62. According to the definition of RC, the corrected activity concentration inside the spheroid by RC method can be calculated by  $A_{spRC} = p/RC_t$ , where  $p$  is the same as in Equation 12.

## RESULTS

### Data Collection

Some activity profiles are shown in Figure 2. When spheroids are smaller than approximately 10 mm in diameter or contrast (OBR) is lower than approximately 10, data in group I and group IIA may be significantly different. The difference comes from three factors: noisier emission and transmission scans and emission-transmission misregistration.

### Fitting of the Adjusting Factors

The adjusting factors obtained by applying Equation 11 to group I data are shown in Figure 3. When the AC is high, the adjusting factors are close to 1. When AC is reduced below 5 for  $f_{gz}$  and 3 for both  $f_{gxy}$  and  $f_{nm}$ , the adjusting factors decrease nearly exponentially with AC.

Two studies in group I with similar OBRs (5.6 and 6.4) are compared in Figure 4 to highlight the effects of randoms ratio. For a given spheroid size and OBR, higher randoms ratio is related to smaller adjusting factors.

The adjusting factors used in fitting and the fitting results are shown in Figure 5. Note that the fitting results for  $f_{gxy}$  and

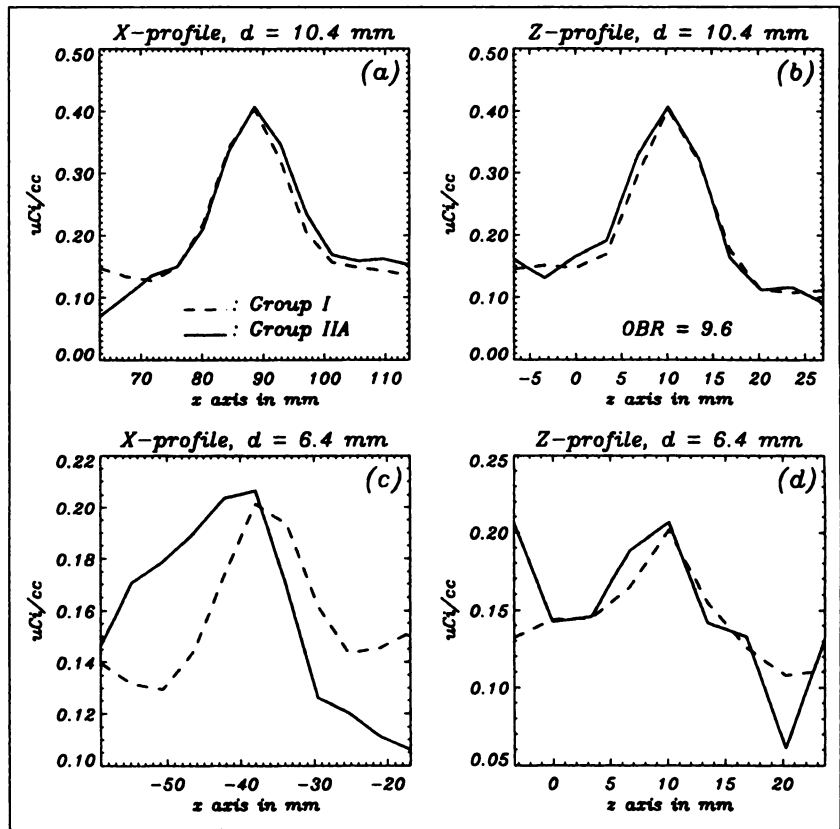


**FIGURE 2.** Activity profiles along x- and z-directions for spheroids with diameters 10.4 mm (A and B) and 6.4 mm (C and D). Contrast is 9.6. Dashed lines are for group I data (nearly ideal data with long emission and transmission scans), and solid lines are for group IIA data (short scans with same phantom, spheroids and OBRs as Group I).

$f_{nm}$  do not appear as a smooth line because the factors depend on both AC and RR, whereas the lines are drawn against AC only. The data for  $f_{gz}$  are much smoother in Figure 6 than in Figure 4 because that is how the three adjusting factors were chosen (see Materials and Methods). The fitted parameters  $k_a, k_b, \dots, k_e$  in Equation 10 are listed in Table 2.

The model-predicted profiles based on the three models (NLSVOD, scaled Gaussian, and AC-RR-adjusted) and group I data are shown in Figure 6. The profiles based on

NLSVOD and scaled Gaussian model are almost indistinguishable. This validates the approximation of Equation 1 with Equation 2. Note that the profiles based on the AC-RR-adjusted model are much closer to the measured data than those based on the other two models, particularly at low apparent contrast.

#### Model-Based Optimization

The fitted spheroid radii and activity concentration of group II data based on the AC-RR-adjusted model are listed

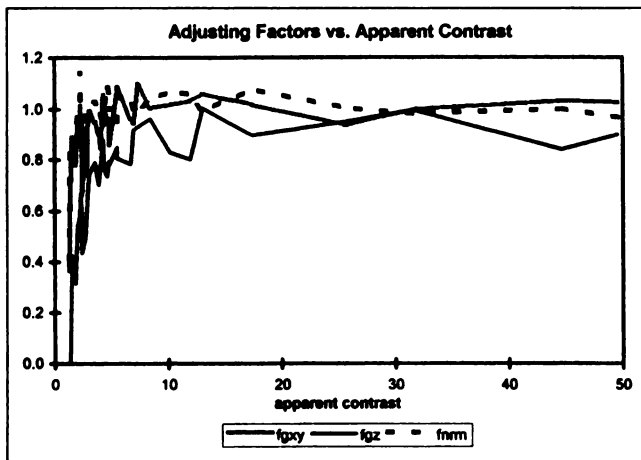


**FIGURE 3.** Adjusting factors are plotted against AC. Note that when AC is less than about 5, factors become significantly smaller than 1.

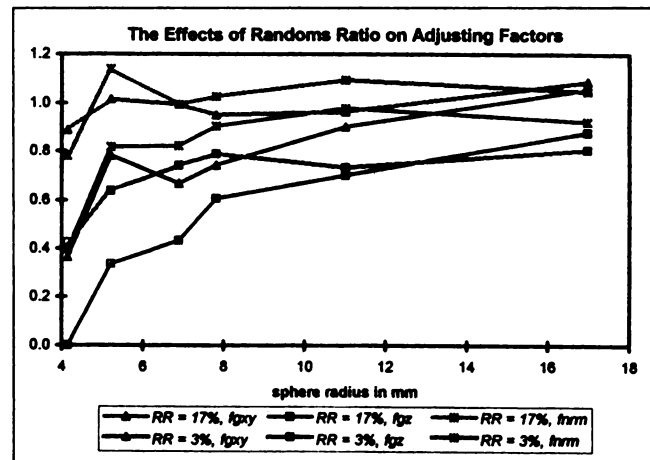


**FIGURE 4.** When OBRs are similar, adjusting factor takes on lower values with higher random ratios (RRs). Note dark line denotes RR. Shaded line denotes different adjusting factors.

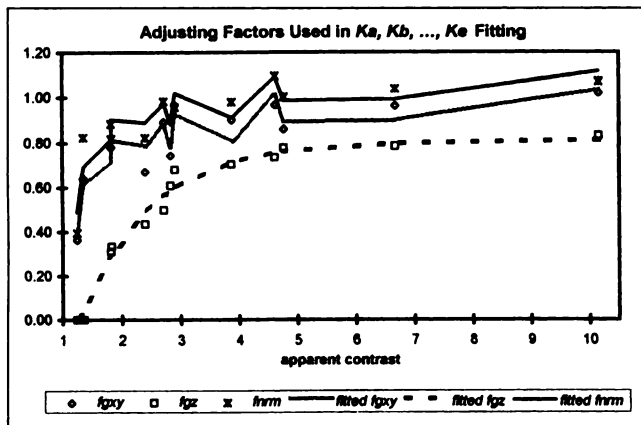


FIGURE 5. Adjusting factors actually used in finding  $k_a, k_b, \dots, k_e$  are shown. Shaded line denotes adjusting factors. Solid line denotes fitted results.

in Tables 3–6. Note that all the activity errors in this manuscript are relative errors in percentage defined as  $A_{sp, measured or corrected} / A_{sp} - 1$ . Activity error reduction in these tables is calculated by subtracting the absolute value of the activity error in the corrected data from that error obtained without correction, i.e., activity error reduction equals  $(1 - RC) - |\text{activity error}_{AC-RR}|$ , where  $|\cdot|$  denotes absolute value. Since  $(1 - RC)$  is the absolute value of activity error without correction, activity error reduction denotes the extent to which the model-based optimization improves quantification. These tables show that for spheroid radii larger than or equal to 6.9 mm, all activity errors are less

TABLE 2  
Fitted Parameters for Adjusting Factors

	$k_a$	$k_b$	$k_c$	$k_d$	$k_e$
$f_{gxy}$	3.53	1.05	39.4	-5.18E-02	1.54
$f_{gz}$	0.830	0.809	0.885	1.17	2.33E-02
$f_{nm}$	3.33	1.13	3.16E-04	3.40	1.40

than 25%, and the radii errors are less than 12%. In general, for spheroid radii between 3.2 and 6.9 mm, the activity and radius errors are less than 35% and 20%, respectively. The maximal  $|\text{activity error}_{AC-RR}|$  for spheroid radii of 5.2, 4.2 and 3.2 mm are 42%, 43% and 59%, respectively. Underestimation of the tracer concentration is significantly reduced by the model-based optimization method in almost all cases despite the relatively larger activity estimation error for smaller spheroids. This is because PVE is relatively large in small spheroids. Also note that, in spite of bubbles, extra fluid and transmission-emission misregistration, the fitting results for group IID are not worse than those for other subgroups in group II data.

By using three-dimensional Gaussian function approximation and Fourier transform as described in theory subsection, we are able to dramatically reduce the computation time for the optimization approach. The parameter estimation for each spheroid required a time range from 2 min for smaller spheroids to 15 min for the largest spheroid on a 300 MHz 21164 Alpha-based Microway workstation (Kingston, MA) running Open VMS (Compaq Computer Corp., Houston, TX).

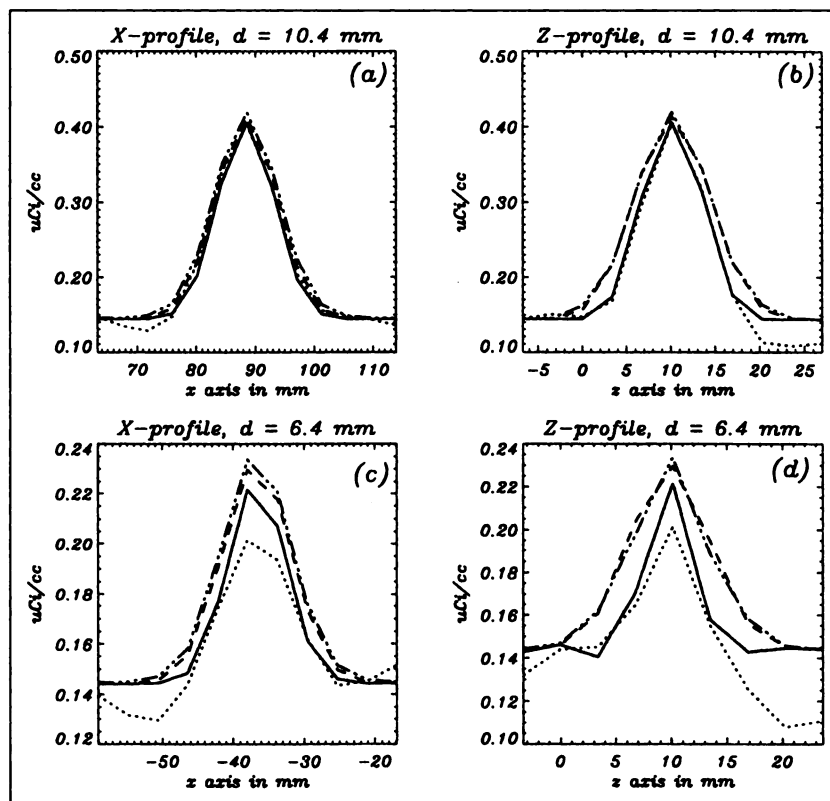


FIGURE 6. Comparison between different models and measured data. Spheroids and OBR are same as in Figure 3. Note that solid line denotes AC-RR-adjusted model, dotted line denotes group I data, dashed line denotes scaled Gaussian model and dash-dot line denotes NLSVOD model. Profiles based on NLSVOD and scaled Gaussian models are similar to each other. Measured data are best described by AC-RR-adjusted model.

**TABLE 3**  
Spheroid Size and Activity Estimation for Group IIA Data Based on AC-RR-Adjusted Model

Reference radius (mm)	OBR			A <sub>sp</sub>			B			OBR			A <sub>sp</sub>			B		
	Fitted activity (kBq/mL)	Fitted activity (mm)	Fitted activity (kBq/mL)	Act. error reduction (%)	Activity error (%)	Radius error (%)	Fitted activity (kBq/mL)	Fitted activity (mm)	Fitted activity (kBq/mL)	Act. error reduction (%)	Activity error (%)	Radius error (%)	Fitted activity (kBq/mL)	Fitted activity (mm)	Fitted activity (kBq/mL)	Act. error reduction (%)	Activity error (%)	Radius error (%)
17	45.0	17	48.5	-2.6	-3.9	5.0	50.5	16	52.9	-3.9	5.0	5.7	50.5	17	50.5	-2.6	-1.6	12
11	48.0	11	54.4	-1.3	7.8	0.35	53.9	11	53.9	-1.1	5.1	28	53.9	11	53.9	-1.1	5.1	19
7.8	46.2	7.9	60.8	-5.0	20	11	60.8	8.1	56.1	3.6	11	30	58.6	7.5	58.6	-3.5	14	34
6.9	44.6	7.0	50.0	0.84	-0.9	57	49.4	7.2	49.4	4.5	-2.0	50	47.7	7.5	47.7	8.7	-7.1	48
5.2	38.0	5.5	45.4	5.2	-10	64	29.3	8.0	29.3	53	-42	23	37.5	6.0	37.5	16	-27	43
4.2	38.7	4.6	34.0	12	-33	50	34.5	4.8	34.5	16	-32	43	29.1	5.1	29.1	22	-43	36
3.2	61.1	2.1	57.9	-18	15	73		2.6	57.9	-18	15	73	51.6	3.3	51.6	3.2	0.57	82

AC = apparent contrast; RR = randoms ratio; OBR = object (spheroid)-to-background radioactivity ratio; A<sub>sp</sub> = radioactivity inside the spheroid; B = background radioactivity; Act. err. reduction = activity error without correction - |activity error|.

**TABLE 4**  
Spheroid Size and Activity Estimation for Group IIB Data Based on AC-RR-Adjusted Model

Reference radius (mm)	OBR			A <sub>sp</sub>			B			OBR			A <sub>sp</sub>			B		
	Fitted activity (kBq/mL)	Fitted activity (mm)	Fitted activity (kBq/mL)	Act. error reduction (%)	Activity error (%)	Radius error (%)	Fitted activity (kBq/mL)	Fitted activity (mm)	Fitted activity (kBq/mL)	Act. error reduction (%)	Activity error (%)	Radius error (%)	Fitted activity (kBq/mL)	Fitted activity (mm)	Fitted activity (kBq/mL)	Act. error reduction (%)	Activity error (%)	Radius error (%)
17	138	17	96.8	-2.1	-10	12	108	17	96.8	-2.6	-3.9	11	108	17	96.8	-2.4	-6.1	15
11	141	11	105	-2.3	-2.2	18	108	11	105	-2.5	8.1	18	108	11	105	-2.5	8.1	29
7.8	134	8.0	101	0.83	-6.4	42	101	7.9	101	4.6	-14	41	77.9	7.9	77.9	1.3	-4.7	45
5.2	139	5.3	107	0.91	-0.84	72	107	5.0	107	-5.0	15	52	73.9	5.5	73.9	5.9	-9.6	61
4.2	136	4.3	134	-12	25	58	134	3.6	134	-9.7	7.6	69	62.0	4.3	62.0	3.9	-24	57
3.2	137	3.1	66.7	20	-38	52	66.7	3.8	66.7	20	-38	52	39.0	3.7	39.0	15	-52	38
2.0	75.2	2.8	48.5	31	-55	40	48.5	2.6	48.5	31	-55	40	41.2	2.4	41.2	19	-50	42

AC = apparent contrast; RR = randoms ratio; OBR = object (spheroid)-to-background radioactivity ratio; A<sub>sp</sub> = radioactivity inside the spheroid; B = background radioactivity; Act. err. reduction = activity error without correction - |activity error|.

**TABLE 5**  
Spheroid Size and Activity Estimation for Group IIC Data Based on AC-RR-Adjusted Model

Reference radius (mm)	OBR = Infinity			OBR = 26.3			OBR = 8.35			OBR = 12.6			OBR = 8.28			OBR = 45.5			OBR = 5.50						
	A <sub>sp</sub>	B	Act. err. reduction (%)	Fitted activity (kBq/mL)	Fitted radius (mm)	Act. err. reduction (%)	Fitted activity (kBq/mL)	Fitted radius (mm)	Act. err. reduction (%)	Fitted activity (kBq/mL)	Fitted radius (mm)	Act. err. reduction (%)	Fitted activity (kBq/mL)	Fitted radius (mm)	Act. err. reduction (%)	Fitted activity (kBq/mL)	Fitted radius (mm)	Act. err. reduction (%)	Fitted activity (kBq/mL)	Fitted radius (mm)	Act. err. reduction (%)				
17	69.7	-1.2	-6.3	14	17	61.3	-1.5	-5.6	14	17	50.7	-2.4	2.7	7.1	17	56.4	-1.7	-1.8	11	17	43.5	-1.1	-4.5	14	
11	76.0	-1.2	2.1	27	11	66.2	-1.1	1.8	25	11	53.3	-0.24	8.0	15	11	60.9	0.038	6.0	18	11	48.5	0.69	6.5	25	
7.8	8.0	73.9	1.8	-0.72	49	8.1	62.6	3.8	-3.7	46	8.4	48.2	7.4	-2.2	44	7.8	64.7	0.17	13	29	8.5	43.2	8.5	-5.2	46
5.2	5.3	77.3	1.6	3.8	70	5.6	58.8	7.1	-9.5	62	5.6	45.8	8.0	-7.1	57	5.2	69.6	-0.17	21	47	6.3	37.6	21	-17	50
4.2	4.4	65.6	5.3	-12	74	4.0	69.2	-3.7	6.5	77	3.2	68.5	-22	39	38	4.7	33.2	14	-42	40	4.1	51.3	-0.91	13	64
3.2	3.4	73.9	5.7	-0.81	91	3.6	49.1	11	-24	64	2.0	60.4	-39	5.2	82										
2.0	4.7	10.8	1.4E2	-85	11	2.6	37.0	27	-43	49															

AC = apparent contrast; RR = random ratio. OBR = object (spheroid)-to-background radioactivity ratio; A<sub>sp</sub> = radioactivity inside the spheroid; B = background radioactivity; Act. err. reduction = activity error without correction - |activity error|.

Figure 7 summarizes |activity error<sub>no correction</sub>|, |activity error<sub>AC-RR</sub>| and the error reduction. Spheroids with radii from 2.0 to 7.8 mm gain the most in quantitative accuracy. The error reduction averaged over spheroids of all sizes is 40% and over 2.0- to 7.8-mm spheroids is 51%. Even the largest two spheroids, of 17- and 11-mm radii, which have relatively small error without PVE correction, have average error reductions of 11% and 22%, respectively. The average |activity error<sub>no correction</sub>| is also the average maximal reducible error for each spheroid size. Note that the average error reduction line is close to this maximal error reducible line for all but the smallest spheroid.

The average |activity error<sub>AC-RR</sub>| for different apparent contrasts is shown in Figure 8. The trend is that the lower the apparent contrast, the higher the average |activity error<sub>AC-RR</sub>|. Table 7 shows that taking |activity error<sub>AC-RR</sub>| ≤ 30% as the acceptable result, then AC = 2.31 is the best threshold in the sense of minimizing type I and type II errors (33).

### Comparison with Scaled Gaussian Method

The fitting results based on the scaled Gaussian model for group IIB are listed in Table 8. These results characterize the fitting problems without using the three adjusting factors. For example, the negative activity error reduction for spheroids with radii of 5.2 and 4.2 mm indicates that errors were increased by the PVE correction.

The averages and standard deviations of activity and radius error for group II data based on AC-RR-adjusted and scaled Gaussian models, and a comparison of the two using a one-tailed paired *t* test are listed in Table 9. Using *P* = 0.05 as the threshold for statistical significance, the AC-RR-adjusted model has significantly smaller activity error than the scaled Gaussian model for spheroids with radii of 11, 7.8, 5.2 and 4.2 mm. For the largest spheroid, 17 mm in radius, the scaled Gaussian model has better activity accuracy than the AC-RR-adjusted model.

### Comparison with Simple RC Method

Activity errors are shown in Figure 9 for the model-based optimization approach and simple RC method with known spheroid radii for three OBRs. This figure contrasts the basic differences between the two approaches. The optimization approach has errors less than 20% for all three OBRs in Figure 9. Although the RC method has relatively comparable activity error for OBR = 9.62, particularly for spheroids with 6.9- to 11-mm radii, it has substantially higher overall errors for OBRs other than 9.62.

The averages and SDs of activity errors for group II data based on AC-RR-adjusted model and RC method (both with known object size), and a comparison of the two using a one-tailed paired *t* test are listed in Table 10. Using *P* = 0.05 as threshold for statistical significance, the AC-RR-adjusted model has significantly smaller activity error than the RC method for spheroids with radii of 11, 4.2, 3.2 and 2.0 mm.

**TABLE 6**  
Spheroid Size and Activity Estimation for Group IID Data Based on AC-RR-Adjusted Model

Reference radius (mm)	OBR					A <sub>sp</sub>					B				
	10.6		45.5		4.29	12.2		47.8		3.93	10.6		45.5		4.29
	Fitted radius (mm)	Fitted activity (kBq/mL)	Radius error (%)	Activity error (%)	Act. err. reduction (%)	Fitted radius (mm)	Fitted activity (kBq/mL)	Radius error (%)	Activity error (%)	Act. err. reduction (%)	Fitted radius (mm)	Fitted activity (kBq/mL)	Radius error (%)	Activity error (%)	Act. err. reduction (%)
17	16	39.9	-5.0	-12	3.7	17	45.4	-2.2	-0.14	15	17	45.4	-2.2	-0.14	15
11	11	45.3	-3.4	-0.43	30	11	48.0	-2.4	5.6	23	11	48.0	-2.4	5.6	23
7.8	7.5	49.0	-4.4	7.6	43	7.7	55.6	-1.3	22	20	7.7	55.6	-1.3	22	20
6.9	6.8	38.7	-0.89	-15	48	6.5	48.9	-5.9	7.4	52	6.5	48.9	-5.9	7.4	52
5.2	5.2	33.5	0.32	-26	50	5.1	49.1	-1.9	8.0	61	5.1	49.1	-1.9	8.0	61
4.2	3.8	45.9	-8.9	0.91	80	4.1	45.6	-0.53	0.16	78	4.1	45.6	-0.53	0.16	78
3.2	2.6	59.5	-18	31	55	2.5	65.9	-21	45	38	2.5	65.9	-21	45	38

Results on the left side of the table are for experiment with bubbles or extra fluid in the spheres.

AC = apparent contrast; RR = randoms ratio; OBR = object (spheroid)-to-background radioactivity ratio; A<sub>sp</sub> = radioactivity inside the spheroid; B = background radioactivity; Act. err. reduction = activity error without correction - |activity error|.

## DISCUSSION

Equation 1 is the most general form for modeling a PET imaging system. This general model can be applied to every work that we know concerning correction of PVE (3,11,12,14,16-28), even though some of them do not have an explicit PSF (3,7-20,24). Almost all of the previous works have implicitly or explicitly neglected the object dependence of the PSF (11,12,14,17-28). Our previously developed NLSVOD model (16) emphasized that object dependence was attributable only to different spheroid (or other targets of interest) locations inside an object, different object geometries and attenuation properties. However, Figures 3 and 4 show that PSF could vary with different radioactivity distributions even when the spheroids have similar location in objects with the same geometry and attenuation properties.

Note that when the adjusting factors  $f_{gxy}$  and  $f_{gz}$  become smaller so that  $f_{gxy}\sigma_{gxy}$  and  $f_{gz}\sigma_{gz}$  also become smaller at low

apparent contrast, it might suggest that the scanner spatial resolution becomes better at low contrast. This is not the case, because the third adjusting factor,  $f_{nm}$ , also becomes smaller. Rather, it implies that the gamma rays from a hot spheroid with low contrast have a lower probability of being detected compared with the gamma rays from the same hot spheroid with high contrast.

We hypothesize that the apparent contrast dependence of the PSF might be related to differences in detection by gamma rays between a hot spheroid and its background; that is, it might be related to the scanner sensitivity discrepancy between a relatively small object and its warm background. We also hypothesize that the dependence of the PSF on random ratios might be attributable to random overcorrection.

Although only hot spheroids in warm or cold background were used in this study, the theory does not require this. Specifically, the proposed method is expected to perform

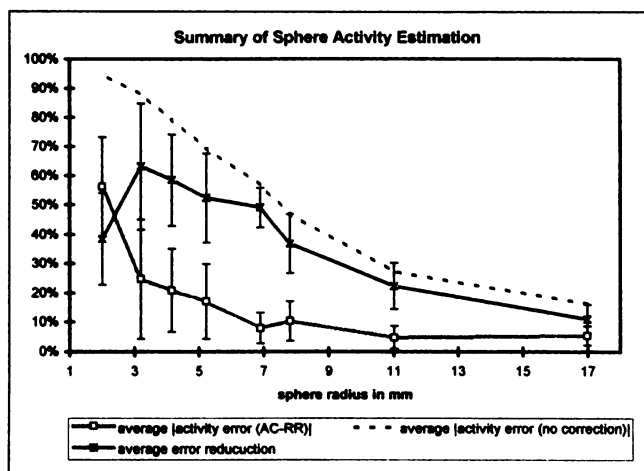


**FIGURE 7.** Average  $|activity\ error_{no\ correction}|$ , average error reduction and average  $|activity\ error_{AC-RR}|$  for different spheroid sizes are shown. Vertical bars denote  $\pm 1$  SD.

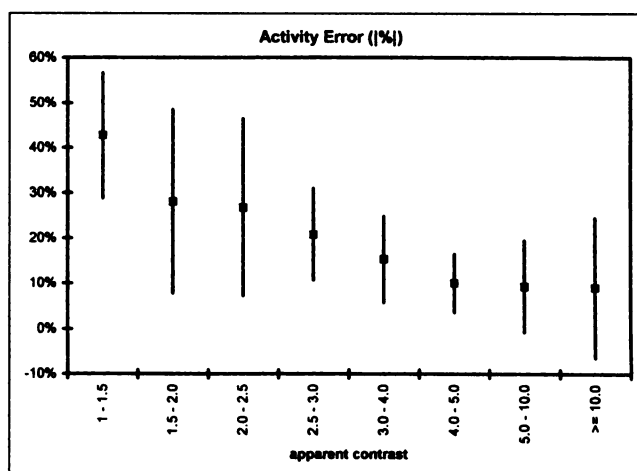


**FIGURE 8.**  $|activity\ error_{AC-RR}|$  is drawn against apparent contrast. Solid squares denote average error, and vertical lines denote  $\pm 1$  SD.

**TABLE 7**  
Acceptable |Activity Error<sub>AC-RR</sub>| and AC Threshold

Acceptable error (%)	Best AC threshold	Type I error (%)	Type II error (%)
30	2.31	8.7	24
45	1.57	1.9	50

AC = apparent contrast; RR = randoms ratio.

equally well for warm or cold spheroids in hot background. We expect that a small cold spheroid will be warmer than predicted using models that do not account for the contrast dependence of the PSF.

Because the AC-RR-adjusted model does not have a scatter part except the scatter scaling factor,  $s_s(O)$ , this model will not be applicable for evaluation of scatter. Under these conditions, the three adjusting factors can be easily incorporated into the NLSVOD model and should be used instead. This also indicates that the best PSF used in scatter correction and image reconstruction (such as maximum likelihood and Bayesian reconstructions) also should depend on apparent contrast.

Spheroid size and activity are correlated parameters. Any sphere much smaller than the PSF effective FWHM will be imaged with a profile that approximates the PSF. Consequently, it can be difficult to distinguish a small spheroid with high activity from a slightly larger spheroid with less activity. The average FWHM of our scanner system PSF, when images are reconstructed with Hann 0.4 cutoff, can be calculated by  $\sqrt{8 \log 2(\sigma_{xy}^2 \sigma_{zz}^2)}^{1/3} \approx 8.7$  mm. To assess the spheroid size limits of our correction, we generated and analyzed noise-free simulation data using the scaled Gaussian models. With noise-free data, the optimization approach can find the correct parameters ( $r$ ,  $\bar{x}_c$ ,  $A_{sp}$  and  $B$ ) for spheroids 3.8 mm or larger in radius. Use of the AC-RR-adjusted model for correction of noise-free data extended the range down to 2.1 mm. Because of this and because we do not expect tumors below this size to be visually conspicuous, we used 2-mm radius as a constraint in the parameter fitting.

The comparison between the results obtained for the scaled Gaussian model with and without the adjusting factors show that these factors are critical for quantitation of spheroids with radii of 5.2 and 4.2 mm. Without the adjusting factors, the optimization approach has a tendency to underestimate the size and overestimate the activity of the spheroid (Table 8). These fits sometimes produce results such that the |activity error<sub>scaled Gaussian</sub>| is even larger than that without any PVE correction for these spheroids (Table 8).

Because of the inclusion criteria of the adjusting factors, the values obtained for  $k_a$ ,  $k_b$ , ...  $k_e$  in Equation 10 would likely underestimate the adjusting factors as a function of AC and RR. Consequently, the effective SDs of the PSF would more likely be underestimated. Tables 7 and 8 show that the adjusting factors obtained in this way prevent the

**TABLE 8**  
Sphere Size and Activity Estimation for Group IIB Data Based on Scaled Gaussian Model

Reference radius (mm)	Infinity				0.00				31.3				108				3.43				8.54				61.1				7.16				16.3				81.7				5.00				7.84				48.5				6.20			
	OBR	$A_{sp}$	B	Act. err. reduction (%)	OBR	$A_{sp}$	B	Act. err. reduction (%)	OBR	$A_{sp}$	B	Act. err. reduction (%)	OBR	$A_{sp}$	B	Act. err. reduction (%)	OBR	$A_{sp}$	B	Act. err. reduction (%)	OBR	$A_{sp}$	B	Act. err. reduction (%)	OBR	$A_{sp}$	B	Act. err. reduction (%)	OBR	$A_{sp}$	B	Act. err. reduction (%)	OBR	$A_{sp}$	B	Act. err. reduction (%)																				
17	149	-1.7	3.1	14	17	105	-2.3	-2.1	20	16	61.8	-3.8	1.1	14	16	81.3	-2.9	-0.45	20	16	46.5	-3.8	-4.2	17	17	149	-1.7	3.1	14	17	105	-2.3	-2.1	20	16	61.8	-3.8	1.1	14	16	81.3	-2.9	-0.45	20	16	46.5	-3.8	-4.2	17							
11	157	-2.0	8.6	22	11	117	-3.6	8.8	21	10	69.7	-6.3	14	12	11	88.6	-3.6	8.5	20	11	48.9	-3.3	0.79	29	11	157	-2.0	8.6	22	11	117	-3.6	8.8	21	10	69.7	-6.3	14	12	11	48.9	-3.3	0.79	29												
7.8	152	0.17	5.5	43	7.6	117	-3.3	8.9	40	6.7	61.3	-14	0.35	54	7.6	82.3	-2.6	0.77	49	7.5	46.7	-3.8	-3.8	47	7.8	152	0.17	5.5	43	7.6	117	-3.3	8.9	40	6.7	61.3	-14	0.35	54	7.6	82.3	-2.6	0.77	49	7.5	46.7	-3.8	-3.8	47							
5.2	170	-4.1	18	57	4.8	132	-7.2	23	50	4.3	92.3	-18	51	17	4.9	96.4	-6.5	18	52	3.8	153	-28	2.2E2	-1.6E2	5.2	170	-4.1	18	57	4.8	132	-7.2	23	50	4.3	92.3	-18	51	17	4.9	96.4	-6.5	18	52	3.8	153	-28	2.2E2	-1.6E2							
4.2	180	-6.6	25	58	3.1	215	-26	1.0E2	-17	3.3	78.2	-21	28	49	3.8	83.6	-8.1	2.4	78	4.1	64.0	-0.39	32	4.2	180	-6.6	25	58	3.1	215	-26	1.0E2	-17	3.3	78.2	-21	28	49	3.8	83.6	-8.1	2.4	78	4.1	64.0	-0.39	32									
3.2	93.1	20	-36	56	3.3	93.2	3.3	-13	77	3.3	41.7	4.0	-32	52	3.9	32.3	23	-60	29	2.3	32.7	12	-60	32	3.2	93.1	20	-36	56	3.3	93.2	3.3	-13	77	3.3	41.7	4.0	-32	52	3.9	32.3	23	-60	29	2.3	32.7	12	-60	32							
2.0	51.9	46	-64	33	2.5	35.3	26	-67	28	2.3	32.7	12	-60	32	2.3	32.7	12	-60	32	2.3	32.7	12	-60	32	2.0	51.9	46	-64	33	2.5	35.3	26	-67	28	2.3	32.7	12	-60	32	2.3	32.7	12	-60	32												

OBR = object (spheroid)-to-background radioactivity ratio;  $A_{sp}$  = radioactivity inside the spheroid; B = background radioactivity; Act. err. reduction = activity error without correction - activity error|.

**TABLE 9**  
Comparison of the Fitting Results Based on AC-RR-Adjusted and Scaled Gaussian Model

Sphere radius (mm)	Activity error					Radius error				
	AC-RR-adjusted		Scaled Gaussian		Paired <i>t</i> test <i>P</i>	AC-RR-adjusted		Scaled Gaussian		Paired <i>t</i> test <i>P</i>
	Average (%)	SD (%)	Average (%)	SD (%)		Average (%)	SD (%)	Average (%)	SD (%)	
17	5.5	3.3	2.8	2.3	0.0022	2.4	1.1	3.0	1.3	2.3.E-05
11	4.8	3.8	12	6.3	2.8.E-06	2.0	2.5	4.7	2.6	5.0.E-06
7.8	10	6.7	16	15	0.033	3.8	3.1	6.2	5.4	0.040
6.9	8.0	5.2	11	6.7	0.22	3.9	3.0	6.7	3.3	0.067
5.2	17	13	43	58	0.047	11	14	13	8.8	0.27
4.2	21	14	44	38	0.017	11	9	18	12	0.058
3.2	25	20	47	71	0.15	18	15	18	13	0.49
2.0	56	17	58	10	0.39	48	49	34	19	0.22

AC = apparent contrast; RR = randoms ratio.

extreme fitting results that cannot be solved easily by applying constraints.

Although Table 9 shows that there is also statistically significant improvement for spheroids between 11 and 6.9 mm in radius and deterioration for the 17-mm spheroid, both the improvement and the deterioration of the AC-RR-adjusted model compared with the scaled Gaussian model for these spheroids are small in any practical sense and can often be ignored. This means for spheroids with radii  $\geq 6.9$  mm (0.8 times the average FWHM), the fitting results are not heavily dependent on the accuracy of the three adjusting factors of the PSF in Equation 9. The deterioration of AC-RR-adjusted model for the 17-mm spheroid may be due to the way the adjusting factors were chosen for the fitting of  $k_a, k_b, \dots, k_e$  as discussed in above.

For spheroids with radii  $\leq 3.2$  mm (0.4 times the average FWHM), the spheroid radius is less than the 3.8-mm limit of the scaled Gaussian model, as stated earlier in this section. Under these conditions, noise, the searching method of the

optimization and initial guess may be more important than an accurate model. This behavior could explain why there is no significant improvement using the adjusting factors for spheroids with radii of 3.2 and 2.0 mm.

The simple RC method depends on the accuracy of the model used to estimate RC, the similarity of the imaging condition to those under which RC is calculated and the accuracy of the size estimate, which is a required input. The consistent S-shaped activity error curves of the RC method in Figure 9 suggest that Equation 13 is not a good model for all spheroid radii. The shift of these S-shaped curves with different OBRs in the same figure clearly shows that the accuracy of the simple RC correction is dependent on OBR with the best results obtained when OBR = 9.62, the values used to determine the parameters  $a$  and  $b$  in Equation 13. Another limitation of the simple RC method is shown in Table 10. Because the RC data for a spheroid with a radius of 2.0 mm was not included in the estimation of  $a$  and  $b$ , the activity error of the RC correction is particularly large for

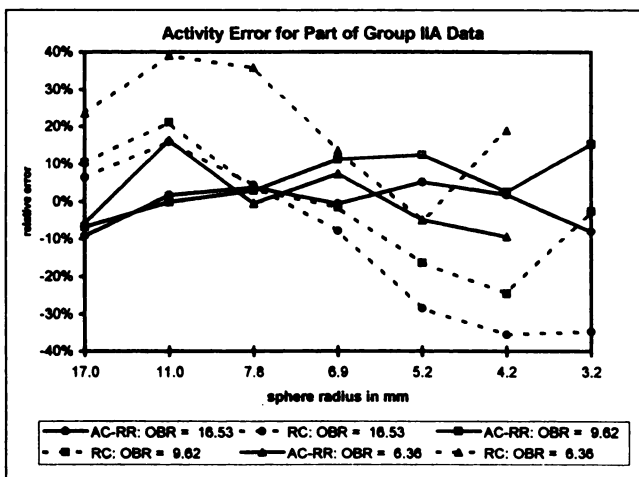


**FIGURE 9.** Comparison of activity errors based on AC-RR-adjusted model and simple RC method. Solid line denotes correction method, and shaded line denotes OBR.

**TABLE 10**  
Comparison of the |Activity Error| of AC-RR-Adjusted Model and RC Method

Sphere radius	Activity error				Paired <i>t</i> test <i>P</i>
	AC-RR-adjusted		RC method		
	Average (%)	SD (%)	Average (%)	SD (%)	
17	8.2	3.2	7.7	6.4	0.41
11	4.6	4.0	17	7.2	7.4.E-07
7.8	8.0	6.3	7.2	9.0	0.38
6.9	7.1	4.0	10	6.0	0.11
5.2	14	14	17	10	0.31
4.2	9.5	11	26	14	0.0033
3.2	12	7.9	34	19	0.0025
2.0	21	15	6.3E2	4.2E2	0.017

AC = apparent contrast; RR = randoms ratio.  
The object (spheroid) sizes are known for both approaches.

this spheroid. Another explanation for the large error of this spheroid is that the RCs for this spheroid are typically small and very sensitive to OBR variation and noise.

Most of the time, the optimization method is able to estimate the spheroid activity and size quite accurately for spheroids larger than 3.2 mm, but there are times that large activity error may occur even for the 5.2-mm radius spheroid. We propose that AC should be used as an indicator, as shown in Table 7 and Figure 8. When high accuracy in activity is required for an *individual* study, it is desirable that AC be larger than 2.31. Otherwise, a priori information such as the spheroid size is needed.

The fact that the fitting results for group IID data are as good as other subgroups in group II presumes that the proposed method is robust under the small violation of the assumption that the hot spheroids are spherical and the radioactivity is homogeneous. It also denotes that transmission-emission misregistration alone does not seem to be a significant limiting factor for the proposed method in this experimental design. We deduce that noise from the emission scan could be a more important factor in this study. This could be because the spheroids were located more than 15 mm from the edges of the phantoms, and the attenuation properties of the phantoms were relatively homogeneous. Another potential limiting factor that has not been addressed in this article is the blurring effect of movement (respiration, heart contraction and patient movement). These factors need further investigation.

## CONCLUSION

The optimization approach is useful for simultaneously estimating the spheroid size and spheroid activity. It significantly improves the activity estimate over a wide range of spheroid size, activity level, OBR and two different phantoms. With appropriate modeling, the model-based optimization is able to simultaneously estimate spheroid activity and size quite accurately for spheroids larger than or equal to 3.2 mm in radius without requiring anatomic data. When the object size is known, this approach substantially improves activity estimation accuracy over the simple RC method.

## ACKNOWLEDGMENTS

This work was supported in part by Grant R29 CA59854 from the National Institutes of Health. We thank Dr. D.L. Wilson for suggesting the no-noise limitation tests. We also would like to thank K.W. Voelker for his excellent work in making and modifying the phantoms, G.P. Leisure for his assistance in performing PET phantom studies, G.J. Muswick for programming advice and Dr. M.S. Berridge, Dr. L. Zheng, B.J. Landmeier and E.H. Cassidy for preparing radiopharmaceuticals.

## REFERENCES

1. Adler LP, Blair HF, Makley JT, et al. Noninvasive grading of musculoskeletal tumors using PET. *J Nucl Med.* 1991;32:1508-1512.

2. Hubner KF, Collmann J, Buonocore E, Kabalka GW, eds. *Clinical Positron Emission Tomography*. St. Louis, MO: Mosby Year Book; 1992.
3. Adler LP, Crowe JP, Al-Kaisi NK, Sunshine JL. Evaluation of breast masses and axillary lymph nodes with [F-18] 2-deoxy-2-fluoro-D-glucose PET. *Radiology.* 1993;187:743-750.
4. Laubenbacher C, Saumweber D, Wagner-Manslau C, et al. Comparison of fluorine-18-fluorodeoxyglucose PET, MRI and endoscopy for staging head and neck squamous-cell carcinomas. *J Nucl Med.* 1995;36:1747-1757.
5. Rodriguez M, Rehn S, Ahlstrom H, Sundstrom C, Glimelius B. Predicting malignancy grade with PET in non-Hodgkin's lymphoma. *J Nucl Med.* 1995;36:1790-1796.
6. Dehdashti F, Mortimer JE, Siegel BA, et al. Positron tomographic assessment of estrogen receptors in breast cancer: comparison with FDG-PET and in vitro receptor assays. *J Nucl Med.* 1995;36:1766-1774.
7. Avril N, Dose J, Janicke F, et al. Assessment of axillary lymph node involvement in breast cancer patients with positron emission tomography using radiolabeled 2-(fluorine-18)-fluoro-2-deoxy-D-glucose. *J Nat Cancer Inst.* 1996;88:1204-1209.
8. Vitola JV, Delbeke D, Meranze SG, Mazer MJ, Pinson CW. Positron emission tomography with F-18-fluorodeoxyglucose to evaluate the results of hepatic chemoembolization. *Cancer.* 1996;78:2216-2222.
9. Rasey JS, Koh WJ, Evans ML, et al. Quantifying regional hypoxia in human tumors with positron emission tomography of [<sup>18</sup>F]fluoromisonidazole: a pretherapy study of 37 patients. *Int J Radiat Oncol Biol Phys.* 1996;36:417-428.
10. Hubner KF, Buonocore E, Gould HR, et al. Differentiating benign from malignant lung lesions using "quantitative" parameters of FDG PET images. *Clin Nucl Med.* 1996;21:941-949.
11. Hoffman EJ, Huang SC, Phelps ME. Quantitation in positron emission computed tomography: 1. Effects of object size. *J Comput Assist Tomogr.* 1979;3:299-308.
12. Kessler RM, Ellis JR Jr, Eden M. Analysis of emission tomographic scan data: limitations imposed by resolution and background. *J Comput Assist Tomogr.* 1984;8:514-522.
13. Nuclear medicine tomography: systems and devices. In: Sorenson JA, Phelps ME. *Physics in Nuclear Medicine*. Philadelphia, PA: W.B. Saunders Company; 1987:424-51.
14. Gambhir S. *Quantitation of the physical factors affecting the tracer kinetic modeling of cardiac positron emission tomography data* [dissertation]. Los Angeles, CA: University of California at Los Angeles; 1990.
15. Keyes JW Jr. SUV: standard uptake or silly useless value? *J Nucl Med.* 1995;36:1836-1839.
16. Chen CH, Muzic RF Jr, Nelson AD, Adler LP. A non-linear spatially-variant object-dependent system model for prediction of partial volume effects and scatter in PET. *IEEE Trans Med Imaging.* 1998;17:214-227.
17. Herrero P, Markham J, Bergmann SR. Quantitation of myocardial blood flow with H<sub>2</sub><sup>15</sup>O and positron emission tomography: assessment and error analysis of a mathematical approach. *J Comput Assist Tomogr.* 1989;13:862-873.
18. Bergmann SR, Herrero P, Markham J, Weinheimer CJ, Walsh MN. Noninvasive quantitation of myocardial blood flow in human subjects with oxygen-15-labeled water and positron emission tomography. *J Am Coll Cardiol.* 1989;14:639-652.
19. Hutchins GD, Caraher JM, Raylman RR. A region of interest strategy for minimizing resolution distortions in quantitative myocardial PET studies. *J Nucl Med.* 1992;33:1243-1250.
20. Feng D, Li X, Huang S-C. A new double modeling approach for dynamic cardiac PET studies using noise and spillover contaminated LV measurements. *IEEE Trans Biomed Eng.* 1996;43:319-327.
21. Henze E, Huang S-C, Ratib O, Hoffman E, Phelps ME, Schelbert HR. Measurements of regional tissue and blood-pool radiotracer concentrations from serial tomographic images of the heart. *J Nucl Med.* 1983;24:987-996.
22. Bol A, Michel C, Melin J, Wijns W. Requisites to modeling of tracer kinetics in the heart using positron emission tomography. In: Beckers C, Goffinet A, Bol A, eds. *Positron Emission Tomography in Clinical Research and Clinical Diagnosis: Tracer Modeling and Radioreceptors*. Boston, MA: Kluwer Academic Publishers; 1989:249-262.
23. Meltzer CC, Leal JP, Mayberg HS, Wagner HN Jr, Frost JJ. Correction of PET data for partial volume effects in human cerebral cortex by MR imaging. *J Comput Assist Tomogr.* 1990;14:561-570.
24. Hatazawa J, Hatano K, Ishiwata K, et al. Measurement of D2 dopamine receptor-specific carbon-11-YM-09151-2 binding in the canine brain by PET: importance of partial volume correction. *J Nucl Med.* 1991;32:713-718.
25. Muller-Gartner HW, Links JM, Prince JL, et al. Measurement of radiotracer concentration in brain gray matter using positron emission tomography: MRI-based correction for partial volume effects. *J Cereb Blood Flow Metab.* 1992;12:571-583.
26. Rousset OG, Ma Y, Leger GC, Gjedde AH, Evans AC. Correction for partial volume effects in PET using MRI-based 3D simulation of individual human brain

- metabolism. In: Uemura K, Lassen NA, Kanno I, eds. *Quantification of Brain Function: Tracer Kinetics and Image Analysis in Brain PET*. New York, NY: Elsevier Science Publishers; 1993:113–125.
27. Sossi V, Buckley KR, Snow BJ, et al. Recovery of the human striatal signal in a slice orientated positron emission tomography. *J Nucl Med*. 1993;34:481–487.
  28. Yu D-C, Huang S-C, Grafton ST, et al. Methods for improving quantitation of putamen uptake constant of FDOPA in PET studies. *J Nucl Med*. 1993;34:679–688.
  29. Spang HA III. A review of minimization techniques for nonlinear functions. *SIAM Rev*. 1962;4:343–365.
  30. Wienhard K, Eriksson L, Grootenk S, Casey M, Pietrzyk U, Heiss W-D. Performance evaluation of the positron scanner ECAT EXACT. *J Comput Assist Tomogr*. 1992;16:804–813.
  31. Brent RP. Real\*8 function Praxis. 1973. Available at: <http://www.netlib.org/opt/praxis>. Accessed Nov. 16, 1998.
  32. A new algorithm for minimizing a function of several variables without calculating derivatives. In: Brent RP. *Algorithms for Minimization Without Derivatives*. Englewood Cliffs, NJ: Prentice-Hall; 1973.
  33. Testing for goodness of fit. In: Zar JH. *Biostatistical Analysis*. Englewood Cliffs, NJ: Prentice-Hall, 1984:40–60.